Journal of Advanced Ceramics
2020, **9**(3): 380–392
https://doi.org/10.1007/s40145-020-0378-5

ISSN 2226-4108
CN 10-1154/TQ

Research Article

A systematic analysis of the radial resonance frequency spectra of the PZT-based (Zr/Ti = 52/48) piezoceramic thin disks

Yu CHEN[a,b], Shaozhao WANG[a], Huajiang ZHOU[a], Qian XU[c], Qingyuan WANG[a,c,*], Jianguo ZHU[b,*]

[a]*School of Mechanical Engineering*, *Chengdu University*, *Chengdu 610106*, *China*
[b]*College of Materials Science and Engineering*, *Sichuan University*, *Chengdu 610065*, *China*
[c]*College of Architecture and Environment*, *Sichuan University*, *Chengdu 610065*, *China*

Received: January 19, 2020; Revised: March 18, 2020; Accepted: March 24, 2020

Abstract: In this paper, both the 1D radial mode and the equivalent circuit of a piezoceramic disk resonator were theoretically analyzed based on IEEE standards. And then, the radial resonance frequency spectra of the PZT-based (Nb/Ce co-doped $Pb(Zr_{0.52}Ti_{0.48})O_3$, abbreviated as PZT–NC) piezoceramic circular disks were measured by an impedance analyzer. A set of resonance frequency spectra including six electrical parameters: *Z*, *R*, *X*, *Y*, *G*, and *B*, were used for making a value distinction between three possible resonance frequencies, and between three possible antiresonance frequencies. A new-form Nyquist diagram was depicted to describe the position relations of these characteristic frequencies. Such a complete resonance frequency spectrum was used to perform the accurate calculation of some material constants and electromechanical coupling parameters for the PZT–NC piezoceramics. Further, the frequency dependence of the AC conductive behavior of the specimen was characterized by the complex impedance measurement. The values of AC conductivity at resonance/antiresonance were deduced from the equivalent circuit parameters. Moreover, the Van Dyke circuit model was assigned to each element contribution and the simulated curves showed a nice fitting with the experimental results. Finally, an additional impedance analysis associated with resonance frequency calculation revealed a complicated coupled vibration mode existing in the annular disk specimen.

Keywords: piezoceramic resonator; radial mode; AC conductivity; resonance frequency spectra

1 Introduction

Since born in 1944 with the discovery of the phenomenon of ferroelectricity, perovskite-type (ABO_3) compounds have been widely used because of their good frequency–temperature response and large electromechanical coupling ability [1]. Although numerous lead-free compositions, based primarily on the $(Na_{1/2}Bi_{1/2})TiO_3$, $(K_{0.5}Na_{0.5})NbO_3$ [2], (Ba,Ca)(Zr,Ti)O_3 [3], and $AgNbO_3$ [4] systems, are actively explored and received increasing attention, $Pb(Zr_{1-x}Ti_x)O_3$ (PZT) is the most widely studied and dominantly used piezoelectric materials till day [5,6]. Its applications can be found in many fields

* Corresponding authors.
E-mail: Q. Wang, wangqy@scu.edu.cn;
J. Zhu, nic0400@scu.edu.cn

such as (i) actuators and sensors for aerospace vibration control, (ii) sonar transducer for naval application, (iii) precision flow control, (iv) fuel injector system, (v) vibration energy harvesting, (vi) biomedical health monitoring, (vii) structural health monitoring, (viii) infrared light detection, (ix) dye wastewater treatment, and (x) other fields [7–9].

The solid solutions of PZT in the vicinity of the morphotropic phase boundary (MPB) remain the most widely used commercially. $Pb(Zr_{0.52}Ti_{0.48})O_3$ is a composition near MPB of $Pb(Zr,Ti)O_3$ that generates anomalously high piezoelectric and dielectric properties. However, almost all useful $Pb(Zr_{0.52}Ti_{0.48})O_3$ ceramics are doped or modified to tailor their properties for specific applications [1,5,6]. The introduction of new piezoelectric ceramics with improved electrical properties usually requires alternatives to the method of determining the material constants associated with radial mode resonance. In the past few decades, numerous authors developed many efficient methods for characterizing the material constants of piezoceramics in the radial model [10–14]. Moreover, some non-analytical methods are also used for identification of the elastic, dielectric, and piezoelectric constants of piezoceramic disk resonators [15,16]. In recent years, the continuous progress of the computer technology has created a specific numerical method, the Finite Element Method (FEM), to iteratively solve the problem of finding the material constants of piezoceramics [17].

By means of the electrical impedance measurement, the characteristics of the equivalent parameters of a Fe/Mn co-doped PZT (PZT-8, "hard") ceramic element embedded in a sanded-cement cubic specimen which is under quasistatic loadings were researched [18]. Such changes in parameters of the PZT ceramic element indicate the stress level according to the relationships between the physical characteristics and the stress. Nowadays, the on-line monitoring or in-service techniques for the civil engineering structures have been developed. PZT-based impedance transducers are widely used for the structural health monitoring (SHM) due to their capability of actuation and sensing [19]. This technique is based on the principle of electromechanical impedance (EMI) in terms of the interaction between the host structure and the piezoceramic transducer where the PZT's electrical impedance is directly related to the structure's mechanical impedance.

In our previous works [20,21], a kind of Nb/Ce co-doped $Pb(Zr_{0.52}Ti_{0.48})O_3$ piezoceramic prepared by a conventional solid-state reaction method has been identified as exhibiting good electrical and mechanical properties, such as a much higher T_C than PIC151 (PI Ceramic, Lederhose, Germany) with a similar d_{33} [22], and a higher d_{33} than PZT-5A with an approached T_C [23], as well as a high compression strength and a high fracture toughness. In this work, some material constants and electromechanical coupling parameters were obtained from the systematic analysis of the radial resonance frequency spectra, which is expected to provide a basis for its further study of SHM using EMI technique.

2 Theoretical analysis

2. 1 Radial resonance mode

For a piezoceramic vibrator, when a harmonic AC electric field is applied to its electrodes with the frequency close to its natural resonance frequency, the mechanical deformation is generated. Thus the resonance in a piezoceramic vibrator involves both electrical and mechanical magnitudes. As shown in Fig. 1, the piezoceramic vibrator is a thin circular disk with a diameter of D (= $2a$) and a thickness of t, whose upper and lower surfaces of the disk are fully covered by electrodes, and poling axis is along the thickness direction. The x_3 coordinate axis is set normal to the circular surfaces in which r and θ are measured. The applied electric field is uniform in the acoustic wave propagation direction. In the nontrivial boundary condition for the planar radial mode, the elastic stress (mechanical stress) T_{rr} is equal to 0 at $r = a$, and the equation of motion for displacement u_r is Bessel's equation.

When a sinusoidal voltage (V) is applied to the piezoelectric ceramic resonator, the current (I) is also sinusoidal with the same angular frequency (ω). The electrical admittance (Y) of the resonator has the form [24]:

$$Y = \frac{I}{V} = \mathrm{j}\omega\frac{\pi a^2}{t}\varepsilon_{33}^{\mathrm{T}}(1-k_{\mathrm{p}}^2) \cdot\left\{1+\frac{k_{\mathrm{p}}^2}{1-k_{\mathrm{p}}^2}\frac{(1+\sigma^{\mathrm{E}})J_1(\eta)}{\eta J_0(\eta)-(1-\sigma^{\mathrm{E}})J_1(\eta)}\right\} \quad (1)$$

where t is the disk thickness, a is the radius, ω is the driving frequency, $\varepsilon_{33}^{\mathrm{T}}$ is the stress-free dielectric constant in the x_3-direction measured at low frequency

$(\varepsilon_{33}^{T}\pi a^2 / t = C_{33}^{T})$, k_p is the standard planar electromechanical coupling factor, σ^E is the Poisson's ratio, and J_0 and J_1 are Bessel's functions of the first kind and zeroth and first order, respectively, subjected to the relation $J_1(z) = zJ_0(z)/J_1(z)$ [25]. η is the product of wave vector ξ and specific resonator dimension a, named the dimensionless wave number.

At resonance, the lossless resonator has an infinitely high admittance ($Y \to \infty$), η satisfies the following transcendental equation:

$$\eta_r \frac{J_0(\eta_r)}{J_1(\eta_r)} = 1 - \sigma^E \tag{2}$$

and at antiresonance ($Y = 0$) we have

$$\eta_a \frac{J_0(\eta_a)}{J_1(\eta_a)} = 1 - \sigma^E - \frac{k_p^2}{1 - k_p^2}(1 + \sigma^E) \tag{3}$$

η_r can be calculated numerically from Eq. (2) for a given σ^E, using the known η_r and the ratio of wave numbers ($\eta_a/\eta_r = f_a/f_r$), k_p could be calculated from the transcendental Eq. (3) as

$$k_p^2 = \frac{(1 - \sigma^E)J_1(\eta_a) - \eta_a J_0(\eta_a)}{2J_1(\eta_a) - \eta_a J_0(\eta_a)} \tag{4}$$

For a given σ^E, the planar elastic modulus c_{11}^p and the elastic compliance S_{11}^E can be calculated as follows:

$$c_{11}^p = \frac{4\pi^2 f_r r^2 \rho}{\eta_r} \tag{5}$$

$$S_{11}^E = \frac{1}{c_{11}^p(1 - (\sigma^E)^2)} \tag{6}$$

Combination of ε_{33}^T, S_{11}^E, σ^E, and k_p can give us the transverse piezoelectric constant d_{31}:

$$d_{31} = k_p \sqrt{\varepsilon_{33}^T s_{11}^E \frac{1 - \sigma^E}{2}} \tag{7}$$

On the other hand, the effective electromechanical coupling factor k_{eff} could be further expressed from the ratio of the resonance and antiresonance frequency. However, due to both transcendental equations for the resonance and antiresonance, k_p has a very complicated relationship with k_{eff}, and their ratio k_p/k_{eff} is a function of σ^E, usually ranging from 1.12 to 1.15 [24].

2.2 Equivalent electrical circuit

In some instances an accurate measurement of the antiresonance frequency cannot be made, and it is then convenient to characterize the resonator by a lumped-parameter equivalent circuit and to calculate the material constants from the measured parameters of this circuit. The former IRE standards on piezoelectric vibrators (IEEE Standard 177-1966) focused on the parameters of equivalent circuit. In the neighborhood of a resonance, the electrical behavior of a piezoceramic vibrator can be described by the Van Dyke circuit model [26] as shown in Fig. 1(b). Such a model has been widely used for representing the equivalent circuit of a piezoelectric vibrator [27,28] and its use was recommended by the IEEE standard on piezoelectricity [29]. This circuit is composed of two shunted branches, one capacitor C_0 and the motional branch formed by resistance R_1, inductance L_1, and capacitance C_1, and the impedance of the Van Dyke circuit model can be expressed as [17]:

$$Z(\omega) = \frac{(1 - \omega^2 L_1 C_1) + j\omega R_1 C_1}{-\omega^2 R_1 C_1 C_0 + j\omega[(C_1 + C_0) - \omega^2 L_1 C_1 C_0]} \tag{8}$$

The Van Dyke circuit model can be used to represent a piezo-electrically excited mechanical vibration system with one dominant resonant mode captured. To capture more modes, the Van Dyke circuit model can be modified and extended with additional RCL branches in parallel

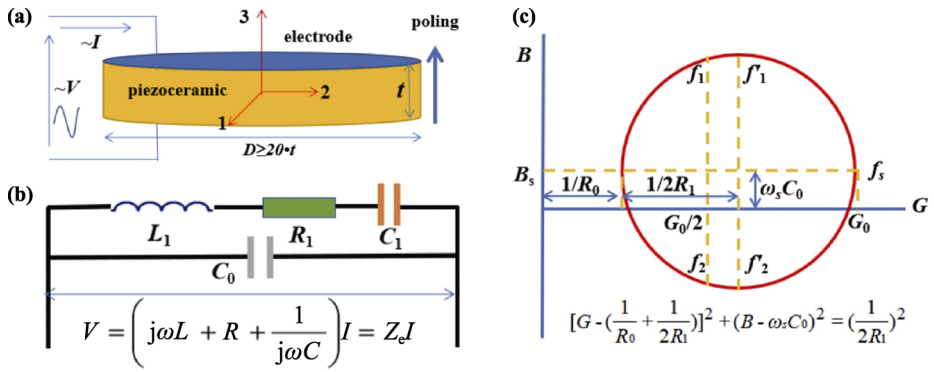

Fig. 1 Theoretical analysis for a piezoceramic circular disk in the radial mode: (a) diagrammatic sketch of the sample, (b) Van Dyke circuit model, and (c) ideal admittance circle.

[30]. It is noted that the derivation of the equivalent circuit parameters requires the modal expansion of Bessel's function in the vicinity of its poles.

For the dominant radial resonant mode of piezoelectric vibrator, the voltage resonance in series circuit corresponds to resonant frequency when $R_1 = Z_{min} = 1/Y_{max}$, while the current resonance in parallel circuit corresponds to antiresonant frequency when $R_1 = Z_{max} = 1/Y_{min}$. The piezoelectric resonator's admittance (Y) is inter-electrode capacity C_0 conductivity produced on antiresonance to resonance determinants ratio [31]. C_0 can be obtained from the following equation [24]:

$$C_0 = \varepsilon_{33}^{T}(1-k_p^2)\frac{\pi a^2}{t} \tag{9}$$

In the lossless resonator, f_1 and f_2 coincide with the admittance and impedance maximum, and each has three associated frequencies, $f_1 \rightarrow (f_m, f_s, f_r)$ and $f_2 \rightarrow (f_n, f_p, f_a)$ corresponding to maximum absolute admittance (impedance), maximum conductance (resistance), and zero susceptance (reactance), respectively [29]. In the case of internal losses, the values of f_m, f_s, and f_r can differ depending on the value of R_1. The same is valid for f_n, f_p, and f_a. If we used a loss resistance R_0 for representing the total dielectric loss of the piezoceramic vibrator subjected to an AC electric field, when the variation amplitude of susceptance is much larger than that of ωC_0, the trajectory of admittance following susceptanc will approximately obey a circle equation with a diameter of $1/R_1$ and a basically settled centre, as shown in Fig. 1(c). However, this is an ideal admittance circle; in fact, with increasing the measuring frequency, its centre tends to move up along the susceptance axis.

In the IEEE standard on piezoelectricity, f_s is defined as the frequency of maximum conductance and f_p is defined as the frequency of maximum resistance. These two important frequencies can be computed as follows [24]:

$$f_s = \frac{1}{2\pi\sqrt{L_1 C_1}} \tag{10}$$

$$f_p = \frac{1}{\sqrt{L_1 \dfrac{C_0 C_1}{C_0 + C_1}}} = f_s\sqrt{1+\frac{C_1}{C_0}} \tag{11}$$

The motional resistance R_1 in the equivalent circuit represents the mechanical dissipation of the piezoelectric resonator. A dimensionless measure of the dissipation is the quality factor Q_m:

$$Q_m = \sqrt{\frac{L_1}{R_1^2 C_1}} = \frac{1}{2\pi f_s R_1 C_1} \approx \frac{f_p^2}{2\pi f_s C_{33}^{T} Z_s (f_p^2 - f_s^2)} \tag{12-1}$$

where Z_s is the impedance at resonance while C_{33}^{T} is the free capacity at 1 kHz. The corresponding accuracy is

$$\theta(Q_m) = Q_m\sqrt{4\theta_r^2(f_p) + \theta_r^2(f_s) + \theta_r^2(C_{33}^{T}) + \theta_r^2(Z_s) + \frac{4}{(f_p^2 - f_s^2)^2}(f_p^4\theta_r^2(f_p) + f_s^4\theta_r^2(f_s))} \tag{12-2}$$

And then the planar electromechanical coupling factor k_p can be calculated as follows

$$k_p^2 \approx 2.51\frac{f_p - f_s}{f_p} - \left(\frac{f_p - f_s}{f_p}\right)^2 \tag{13-1}$$

The corresponding accuracy is

$$\theta(k_p) = \frac{1}{2k_p}\left(2.51 - 2\frac{f_p - f_s}{f_p}\right) \cdot \left(\frac{f_s}{f_p}\right)\sqrt{\theta_r^2(f_p) + \theta_r^2(f_s)} \tag{13-2}$$

However, the relative difference in the frequencies f_s and f_p depends on both the material coupling factor and the resonator geometry. For this reason a quantity called the effective coupling factor (k_{eff}) has been used, not dependent on the specific vibration mode boundary conditions, as a convenient measure of this difference [17,24,29]:

$$k_{eff}^2 = \frac{f_p^2 - f_s^2}{f_p^2} \approx \frac{f_a^2 - f_r^2}{f_a^2} \tag{14}$$

The electromechanical coupling coefficient is an important characteristic of piezoceramic elements used to measure the energy conversion efficiency. Also, the resonator figure of merit M is defined in terms of k_{eff} and Q_m as follows:

$$M = \frac{k_{eff}^2 Q_m}{1 - k_{eff}^2} \tag{15}$$

When k_{eff} is small, this reduces to the definition given M in IEEE Standard 177-1978.

On the other hand, the planar electromechanical coupling factor k_p can be also related to the transversal electromechanical coupling factor k_{31} with the participation of Poisson's ratio σ^E:

$$k_{31} = k_{\mathrm{p}}\sqrt{\frac{1-\sigma^{\mathrm{E}}}{2}} \tag{16}$$

3 Experimental procedures

The specimen selected for the experiment is a kind of Nb/Ce co-doped PZT ceramics with a chemical formula of $Pb(Zr_{0.52}Ti_{0.48})_{0.95}Nb_{0.05}O_3$+0.2wt%$CeO_2$ (PZT–NC), which were fabricated by a conventional solid-state reaction from oxide precursors and sintered at 1225 ℃ for 2 h in a sealed crucible before [19]. To illustrate the determination of the resonance frequencies and the use of the Van Dyke circuit model for the PZT–NC piezoceramics, two kinds of specimens: circular disks (D (~10 mm) × t (~0.5 mm)) and annular disks (D_0 (~10 mm) × D_i (~4 mm) × t (~0.5 mm)) were prepared in this experiment. After poling along the thickness direction, the electrical impedance with stress-free boundary conditions was measured for these specimens between 80 and 560 kHz using an impedance analyzer (PV70A, Beijing Band Era Co., LTD, Beijing, China). Measurements were made at room temperature with an applied voltage of 1 V. The equivalent circuit parameters were determined by fitting the impedance curve using the Z-View software (version 3.1, Scribner Associates, Inc.). Figure 2 shows the computing frame of material constants and electromechanical coupling parameters of piezoceramics from the impedance measurement in the radial mode.

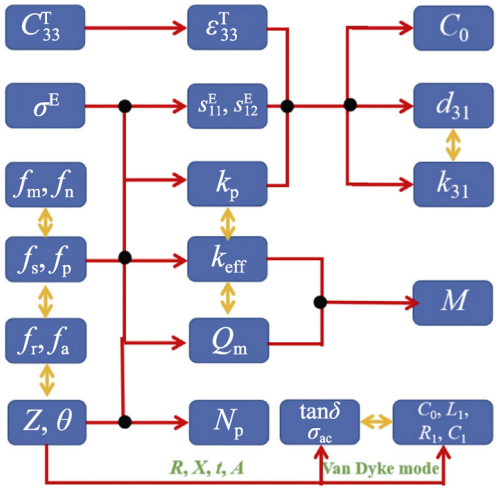

Fig. 2 Computing frame of material constants and electromechanical coupling parameters of pizeoceramics based on the impedance measurement in the radial mode.

4 Results and discussion

The determination of the resonance frequencies for the circular disk specimen is shown in Fig. 3. Around the resonance frequency, the electrical admittance Y is a complex function of ω (Fig. 3(a)), whose real and imaginary parts are conductance G (Fig. 3(b)) and susceptance B (Fig. 3(c)), respectively (i.e., $Y = G + \mathrm{i}B$). An ascending order of f_{m} (228.72 kHz) < f_{s} (228.843 kHz) < f_{r} (228.956 kHz) can be observed from the locus (Fig. 3(d)) that plots the relative variation between G and B. The mean power supplied

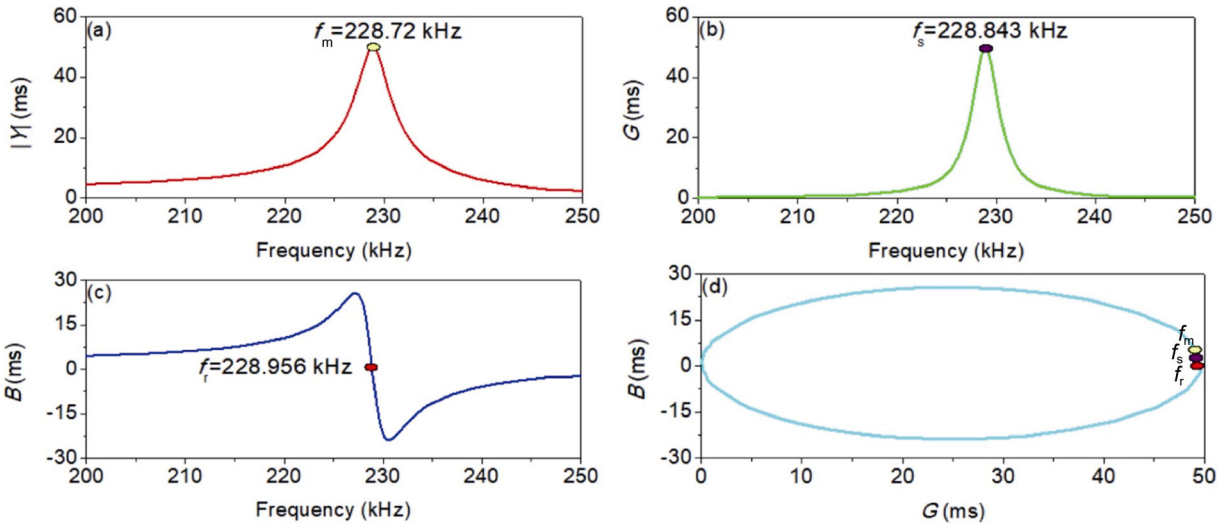

Fig. 3 Determination of the resonance frequencies for the circular disk specimen: (a) maximum admittance modulus, (b) maximum electric conductance, (c) zero susceptance, and (d) polar representation.

by the voltage source and consumed by the impedance is proportional to conductance G. For that reason, the maximum of G is associated to the series resonance frequency (f_s), even in the case of coupling modes. For the disk vibrator, the planar radial frequency constant N_p is the product of the series resonance frequency and the disk diameter ($N_p = f_s \cdot D$). This factor is calculated to be 2105 Hz·m for PZT–NC piezoceramics.

Figure 4 shows the determination of the antiresonance frequencies for the circular disk specimen. As can be seen, Z is also a complex number (Fig. 4(a)), and its real and imaginary parts are resistance R (Fig. 4(b)) and reactance X (Fig. 4(c)), respectively (i.e., $Z = R + jX$). A descending order of f_n (270.02 kHz) > f_p (269.584 kHz) > f_a (269.076 kHz) is revealed by the R–X locus (Fig. 4(d)). The maximum of R is associated to the parallel resonance frequency (f_p). Here, both three possible resonance frequencies and three possible antiresonance frequencies are presented in the G–B locus and the R–X locus, respectively. For lossless resonators, these frequencies are close, but the difference is very important for lossy and/or weak resonators.

According to the electroelastic theory of dielectrics, the imaginary parts of the elastic compliance and dielectric permittivity represent the mechanical and electrical losses, respectively. Thus the dielectric loss factor (tanδ) can be computed as the ratio between the real and the imaginary parts of the admittance or impedance.

$$\tan\delta = \frac{G}{|B|} = \frac{R}{|X|} \tag{17}$$

The frequency dependence of the dielectric loss factor of the circular disk specimen is shown in Fig. 5. Such two tandem loss peaks can be related to the resonance and antiresonance responses of the sample, respectively. However, the antiresonance response excited a weaker loss peak. As we knew, both electrical and mechanical magnitudes are involved with the resonance response in a piezoceramic vibrator. In the frequency range of impedance measurement, the increases in motional reactance and stiffness are fundamentally dependent on the mean stress <T> [32]. In comparison to resonance, the increased reactance at antiresonance may be responsible for the decreased loss in this case. On the other hand, due to the multidomain structure of piezoceramics, both domain wall motion and interaction between ferroelectric domains and lattice defects could cause internal friction, which has been considered as the origin of the elastic (mechanical) losses of ferroelectric ceramics. During resonance/antiresonance, both the domain wall oscillation caused by the alternating field and the domain wall motion caused by the mechanical deformation can be connected with the conductivity, which is a major contributor for the dielectric losses of ferroelectric ceramics [33]. For the PZT–NC piezoceramics used in the impedance measurement, tanδ is evaluated to be 3.10% at 100 kHz. As expected in this donor doped

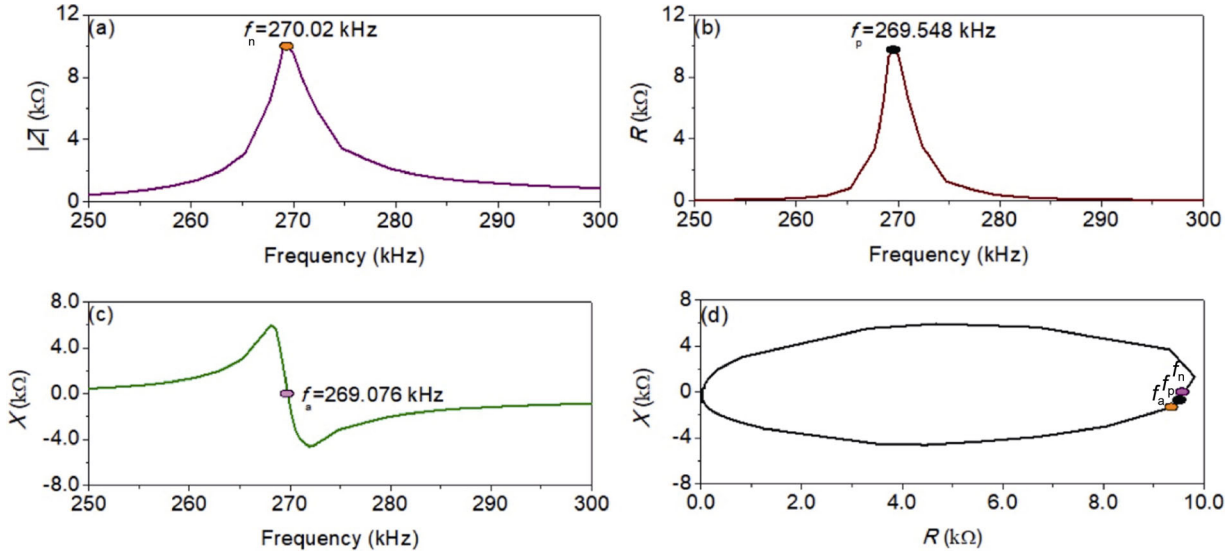

Fig. 4 Determination of the antiresonance frequencies for the circular disk specimen: (a) maximum impedance modulus, (b) maximum electric resistance, (c) zero reactance, and (d) polar representation.

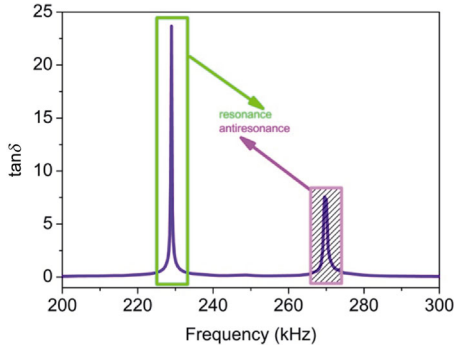

Fig. 5 Frequency dependence of the dielectric loss factor of for the circular disk specimen.

PZT, its loss value is higher than those of the pure (undoped) PZT ceramics (tanδ ≈ 1.1%) [34]. With respect to the undoped PZT, which behaves as weakly hard, donors like high-valence Nb^{5+} and Ce^{4+} did not only make the domain wall motion easier but also introduced defects like Pb vacancies in the PZT lattice [35]. As a result, an increased dielectric loss was observed in the Nb/Ce co-doped PZT piezoceramics.

The complex impedance of piezoelectric resonator is given by the following equation set Eqs. (18)–(21) [24]:

$$Z(\omega) = R(\omega) + \mathrm{j}X(\omega) \tag{18}$$

$$R(\omega) = \frac{1}{\omega C_0}\frac{\omega\omega_s Q_m(\omega_p^2-\omega_s^2)}{\omega^2\omega_s^2 + Q_m^2(\omega^2-\omega_p^2)^2} \tag{19}$$

$$X(\omega) = -\frac{1}{\omega C_0}\frac{\omega^2\omega_s^2 + Q_m^2(\omega^2-\omega_s^2)(\omega^2-\omega_p^2)}{\omega^2\omega_s^2 + Q_m^2(\omega^2-\omega_p^2)^2} \tag{20}$$

$$|Z(\omega)| = \frac{1}{\omega C_0}\sqrt{\frac{\omega^2\omega_s^2 + Q_m^2(\omega^2-\omega_s^2)^2}{\omega^2\omega_s^2 + Q_m^2(\omega^2-\omega_p^2)^2}} \tag{21}$$

As mentioned above, resonance f_r and antiresonance f_a frequencies are the solution of equation $B = 0$ and $X = 0$, respectively. Frequency f_m at minimum and f_n at maximum impedance ($f_m < f_r < f_a < f_n$) are the solution of equation $\partial Z/\partial f = 0$, while the last equation for the minimum and maximum impedance could not be analytically solved, there are some estimates for these characteristic frequencies [36]):

$$f_m \approx f_s\sqrt{1+\frac{1}{2r}\left(1-\sqrt{1+\frac{4r^2}{Q_m^2}}\right)} \tag{22}$$

$$f_r \approx f_s\sqrt{1+\frac{1}{2r}\left(1-\sqrt{1-\frac{4r^2}{Q_m^2}}\right)} \tag{23}$$

$$f_a \approx f_s\sqrt{1+\frac{1}{2r}\left(1+\sqrt{1-\frac{4r^2}{Q_m^2}}\right)} \tag{24}$$

$$f_n \approx f_s\sqrt{1+\frac{1}{2r}\left(1+\sqrt{1+\frac{4r^2}{Q_m^2}}\right)} \tag{25}$$

$$f_p = f_s\sqrt{1+\frac{C_1}{C_0}} = f_s\sqrt{1+\frac{1}{r}},\quad r = \frac{C_0}{C_1} = \frac{1}{k_{eff}^2} - 1 \tag{26}$$

Figure 6 shows the fundamental resonance and antiresonance frequencies of the circular disk specimen in the radial mode. It can be seen that the estimated error of all these characteristic frequencies are limited within 0.2%, in the case of using the approximate equations above. Further, based on the form of Eqs. (22)–(25), a uniform expression as follows is proposed here for them:

$$f \approx f_s\sqrt{1+\frac{1}{2r}\left(1+a\sqrt{1+b\frac{4r^2}{Q_m^2}}\right)} \tag{27}$$

If we defined $a = -1, +1$, while $b = 0, -1$, and $+1$ here, the position relations between these characteristic frequencies can be depicted by a Nyquist diagram according to the equation above. For a low loss material $f_1 \approx f_m \approx f_s \approx f_r$ and $f_2 \approx f_a \approx f_p \approx f_n$, but for a lossy material these values differ from each other as follows:

$$f_m < f_s < f_r < f_a < f_p < f_n \tag{28}$$

$$(f_n - f_m) > (f_p - f_s) > (f_a - f_r) \tag{29}$$

For piezoceramics with high coupling factor (k_{eff}) and reasonably high mechanical (Q_m), the value of $4r^2/Q_m$ shifts towards to zero, and then the differences between

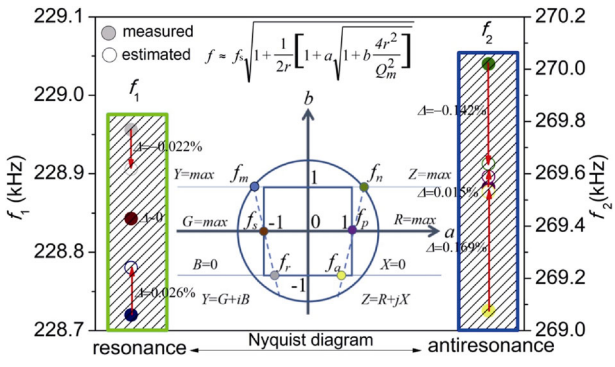

Fig. 6 Fundamental resonance and antiresonance frequencies of the circular disk specimen (the insert is a new-form Nyquist diagram depicted by the approximate equation).

those three frequencies in the same side are nearly equal.

$$f_r - f_s \approx f_s - f_m \tag{30}$$

$$f_n - f_p \approx f_p - f_a \tag{31}$$

which can be understood by the slope of the two secant lines (f_m—f_s—f_r and f_a—f_p—f_n) in the Nyquist circle. After knowing the difference between f_s and f_p, the values of k_p and k_{eff} can be calculated to be 60% and 53% from Eqs. (13) and (14), respectively. In fact, the most complicated relationship is between the effective coupling factor k_{eff} and the planar coupling factor k_p due to both transcendental equations for the resonance and antiresonance. However, using the (f_m, f_n) frequency pair leads to significant errors in the coupling (k) and piezoelectric coefficient (d). While using the (f_s, f_p) frequency pair gives reasonable agreement with PRAP for the coupling (k) [37].

Further, the complete resonance spectra of the circular disk specimen are presented in Fig. 7. For a thin circular disk, its fundamental radial resonance mode should produce a pair of resonance–antiresonance peaks in this frequency range. In Fig. 7(a), the impedance (top curve) drops to a minimum at the resonant frequency and rises to a maximum at the antiresonant frequency. The phase (bottom curve) rises to a maximum value of 83.6° roughly at the center of the resonance. A high angle indicates the fully poled state of the specimen. For modes where the mechanical movement is perpendicular to the direction of the electrical excitation, e.g., length expansion of thin bars thickness poled or radial modes of thickness poled thin discs, the mechanical resonance corresponds to the minimum of the electrical impedance, i.e., the electrical resonance. This is due to the fact that the electric open/short circuit conditions are interchanged with the mechanical ones [38]. Full impedance spectrum for the piezoelectric resonator at resonance reflects also the resonator mechanical quality defined by the mechanical quality factor Q_m. It could be calculated from the impedance spectroscopy at resonance as

$$Q_m = \frac{f_r}{\Delta f} \tag{32}$$

where $\Delta f = f_2 - f_1$ and f_r, f_1, and f_2 are the frequencies at the resonance and at 3 dB value of the impedance at resonance (i.e., at the values of frequency where the impedance is equal to $Z/\sqrt{2}$). From Fig. 7(b) the resolution for the impedance resonance peak gives Q_m the value of 69.

As shown in Fig. 7(c), the variations of both admittance and phase with frequency are quite opposite to that of impedance/phase. In addition to the equation above, there is another computational formula proposed for Q_m in terms of

$$Q_m \approx \frac{f_r}{f_+ - f_-} \tag{33}$$

Here, f_+ and f_- are the upper and lower half power frequencies, respectively. For high Q_m resonators Eq. (33) becomes equal. In practice, for Q_m higher than 10, it differs in less than 0.1%. These values can be used in the optimization algorithm as the initial shot. Figure 7(d) shows the determination of f_+ and f_- from the admittance resonance curve. The value of Q_m is

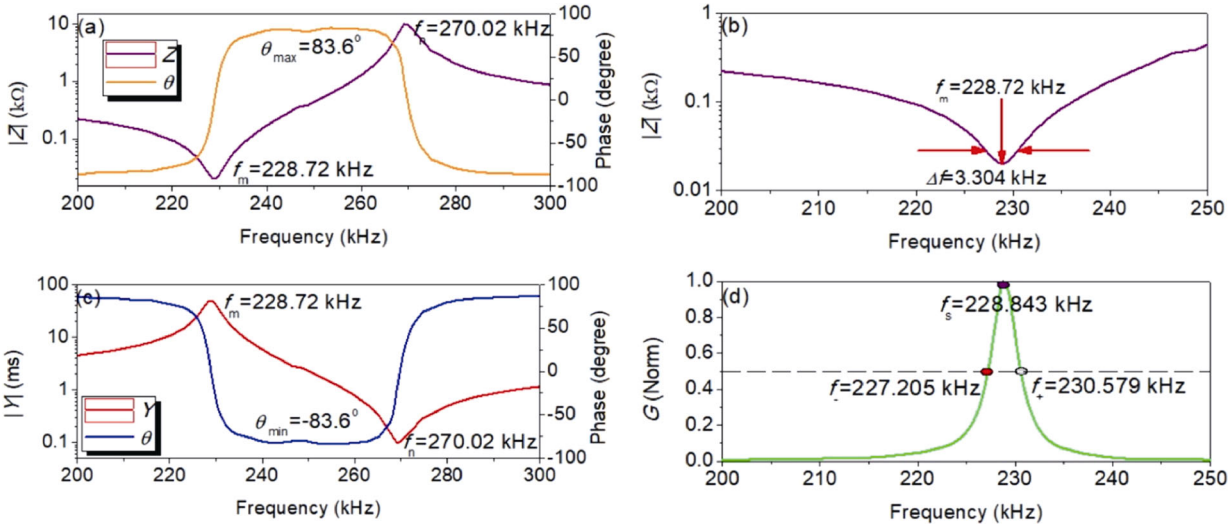

Fig. 7 Complete resonance frequency spectra of the circular disk specimen: (a) impedance and phase curves, (b) impedance resonance peak, (c) admittance and phase curves, and (d) conductance resonance peak.

calculated to be 68. In the case of k_{eff} = 0.53, the value of M can be determined as 27 according to Eq. (15). Here, $5 < M < 50$, which demonstrates that the use of f_p and f_s in this experiment is better to calculate the electromechanical coupling coefficient for the PZT–NC piezoceramics than f_m and f_n.

Figure 8 shows the complex impedance spectrum of the circular disk specimen at 80–560 kHz. The complex impedance plots Z' versus Z'' (arc), where Z' and Z'' are the real and the imaginary parts of the complex impedance (Z). Usually, three distinct arcs may be observed in polycrystalline ceramics. With increasing frequency from right to left side of the Z' axis, arcs 1, 2, and 3 in succession can be attributed to the electrode effect, the grain-boundary effect, and the grain or bulk effect, respectively [39]. From Fig. 8, the center of the experimental arc seems to be located at the real axis, and there is only a semicircular arc presented. Therefore, the electrical contribution of specimen is from only grains (bulk materials). The AC bulk conductivity is evaluated from the following equation [40]:

$$\sigma_{ac} = \frac{Z'}{Z'^2 + Z''^2}\frac{t}{A} \tag{34}$$

where σ_{ac} is the AC conductivity, t is the thickness, and A is the area, Z' and Z'' are the real and imaginary parts of the impedance, respectively, $Z' = R(\omega)$, $Z'' = X(\omega)$, and $Z'^2 + Z''^2 = |Z(\omega)|^2$. By combing Eqs. (10)–(12) and Eqs. (19)–(21), the AC conductivity can be expressed as a function of the frequency by the following equation:

$$\sigma_{ac} = \frac{\omega^2\omega_s^2}{R_1\left[\omega^2\omega_s^2 + Q_m^2(\omega^2 - \omega_s^2)^2\right]}\frac{t}{A} \tag{35}$$

As can be seen from the equation above, for the piezoceramic resonator with a certain dimension at resonance ($\omega = \omega_s$), σ_{ac} depends only on R_1. While at antiresonance ($\omega = \omega_p$), by using the expression of Q_m with equivalent circuit parameters (Eq. (12)), Eq. (35) can be further simplified to be as follows:

$$\sigma_{ac} = \frac{R_1C_0^2\omega_p^2}{R_1^2C_0^2\omega_p^2 + 1}\frac{t}{A} \approx R_1C_0^2\omega_p^2\frac{t}{A} \tag{36}$$

With the help of the complex impedance measurement, the frequency dependence of the AC conductivity of the circular disk specimen is depicted in Fig. 9. As marked by the green rectangular box, the measured σ_{ac} shows the maximum value of 3.47×10^{-3} S/cm at resonance and the minimum value of 6.46×10^{-3} S/cm at antiresonance. According to the equivalent circuit parameters (R_1 = 19.65 Ω and C_0 = 1.365 nF) obtained subsequently, the values of σ_{ac} at resonance and antiresonance are calculated to be 3.24×10^{-3} and 6.7×10^{-6} S/cm. Such a very small deviation between measured values and calculated values demonstrates the usability of Eq. (35) for predicting the AC conductivity of the piezoceramics at resonance/antiresonance in terms of their equivalent circuit parameters.

Above the antiresonance frequency, the frequency dependence of the conductivity follows the double power law instead of simple Jonscher's power law [41].

$$\sigma(\omega) = \sigma(0) + A\omega^{s_1} + B\omega^{s_2} \tag{37}$$

where $\sigma(\omega)$ is the AC conductivity, ω is the angular frequency ($\omega = 2\pi f$), $\sigma(0)$ is the frequency independent conductivity. As shown in the inserted figure, fitting of the experimental data yields values of s_1 and s_2 as 0.39 and 0.65, respectively. For the PZT–NC piezoceramic resonator measured in a frequency range of 88–560 kHz, hence, its AC conduction mechanism in the region above the antiresonance frequency could be attributed

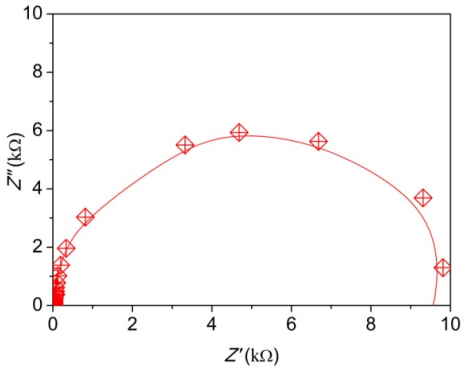

Fig. 8 Complex impedance spectrum of the circular disk specimen between 80 and 560 kHz.

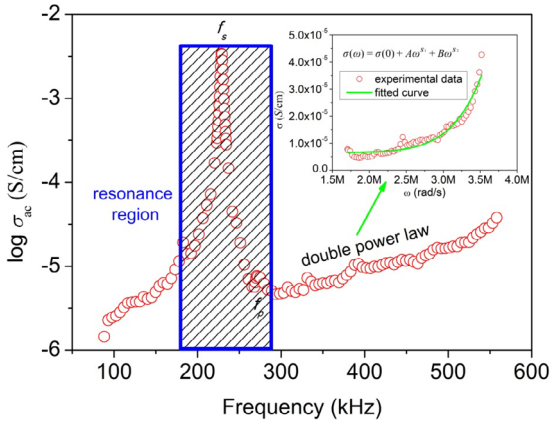

Fig. 9 Frequency dependence of the AC conductivity of the circular disk specimen.

to the mixture of the translational hopping motion and the localized orientation hopping [42].

For transducer applications, it is sometimes more convenient to fit the impedance plots to lumped circuit models in order to predict the electrical behavior of the resonator. The response curves of the electrical impedance and phase angle of the circular disk specimen are shown in Fig. 10. Both these two curves were fitted by the Van Dyke circuit model with consideration of energy dissipation. However, it can be observed from Fig. 10(a) that the error of fitting for the antiresonance impedance amplitude is larger than that for the resonance impedance amplitude. Under the 1D model, resonance amplitudes depend on elastic losses only while antiresonance amplitude depends on elastic losses mainly, as well as the participation of both dielectric and piezoelectric losses [43]. However, under 3D model, the piezoelectric constants and dielectric permittivity are lossless, and both resonances and antiresonances are govern by elastic losses [44,45].

Here, the classical Van Dyke circuit model uses four real circuit parameters, C_0, C_1, L_1, and R_1 to represent the impedance of a free standing piezoelectric resonator around resonance. In this experiment, one-dimensional (1D) approximation for the simple vibration modes (fundamental resonance and its overtones) is used for the derivation of equivalent circuit parameters. The equivalent circuit parameters derived from the 1D mode are inserted in Fig. 10(a). The value of C_1/C_0 is evaluated to be 0.39, such a high value corresponding to the broadening frequency bandwidth of the resonance peak. And the loss component R_1 is related to the speed that the resonance peak decays. A smaller value of ~20 Ω indicates a slower decaying speed of the resonance peak.

It can be seen from Fig. 10(b) that, the phase angle is much close to –90° but not fully equal to –90° before resonating. Such a result indicates that the piezoceramic resonator behaves in a property of a capacitor in the case of no resonance. And there is a little energy dissipation existing in the specimen subjected to the electric loading. In the resonance region (220–280 kHz), the decreased phase angle (~80°) can be related to the energy dissipation caused by resonance. In fact, the physical meanings of these four components modeled for the equivalent circuit can be understood by the equivalent structure of a piezoelectric element. As shown in Fig. 11, the component C_0 represents its dominant capacitance; while the components L_1, R_1, and C_1 are relevant to its equivalent mass m_e, damping

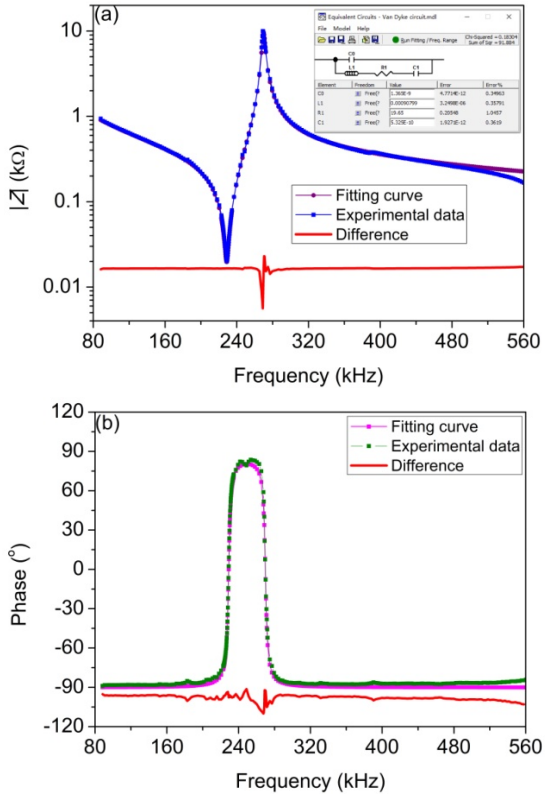

Fig. 10 Fitting of the resonance frequency spectra of the circular disk specimen according to the Van Dyke circuit model: (a) impedance curve; (b) phase curve.

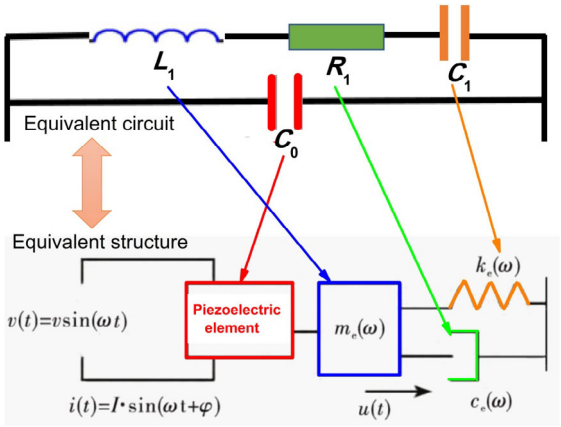

Fig. 11 Correlations between the equivalent circuit and the equivalent structure of a piezoceramic resonator.

coefficient c_e, and spring constant k_e, respectively.

Some material constants and electromechanical coupling parameters were calculated for the specimen from the measured frequency data according to the corresponding equations shown in Section. 2. The calculated data are listed in Table 1 and compared with the measured data derived from the instrument. A very small deviation is observed from the comparison between

Table 1 Elastic, piezoelectric, and electromechanical coupling parameters of the PZT–NC piezoceramics

Parameter	s_{11}^E	s_{12}^E	σ^E	N_p	d_{31}	k_{31}	k_p	k_{eff}	Q_m	M	C_0
	(10^{-12}m^2/N)		(—)	(Hz·m)	(pC/N)	(%)	(%)	(%)	(—)	(—)	(nF)
Value	15.02	4.96	0.33	2106	161	35	60(59)	53(53)	69(68)	27(27)	1.37(1.53)

Note: the contents included in the brackets represent the measured values, and others are the calculated values.

the calculated and measured electromechanical properties (k_p, k_{eff}, Q_m, and M). Especially, the high k_p of 0.60 is expected to be used for some piezoelectric devices requiring a high electromechanical transform ability. Also, it means that having perfect elastic or dielectric properties, piezoceramics have perfect electroelastic properties too.

Figure 12 shows the resonance frequency spectrum of the annular disk specimen between 120 and 200 kHz. As marked by the yellow rectangular box, there are two pairs of resonance–antiresonance peaks whose frequencies are adjacent appearing in the impedance curve, and the corresponding phase angle at resonance reaches to only ~60°. This resonance spectrum significantly differs from that of the circular disk specimen, indicating that the resonant vibration may be not a single mode.

According to Huang *et al.*'s theory [46], the radial extensional resonance and antiresonance frequencies for the piezoceramic annular disks with traction-free boundary conditions can be expressed as

$$f = \frac{\eta}{2\pi R_0}\sqrt{\frac{1}{\rho s_{11}^E(1-\nu_p^2)}} \tag{38}$$

where η is the frequency parameter of the radial (extensional) vibration, which is a function of the inner-to-outer radius ratios (α) of the annular disk. For the PZT–NC piezoceramic annular disk measured: α = 0.4, $f_{r,a}$(average) = 155.66 kHz. Therefore, η was

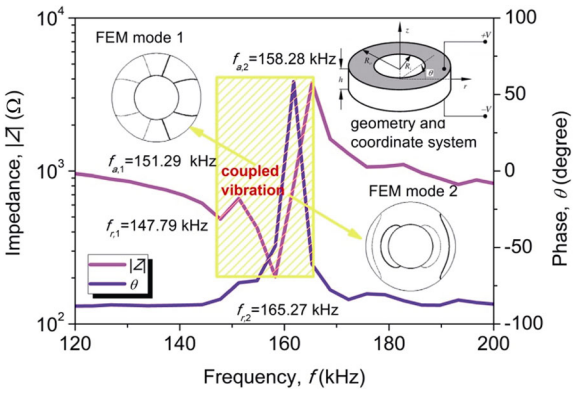

Fig. 12 Resonance frequency spectrum of the annular disk specimen between 120 and 200 kHz

evaluated to be 3.05 from the equation above, which is between 1.7 for the FEM (Finite Elements Method) mode 1 and 5.5 for the FEM mode 2. In addition of a lower phase angle, the resonant vibration of the annular disk specimen may be considered as a coupling between these two vibration modes. It is the coupling inside the material which modifies the resonance conditions and not the geometrical dimensions of the vibrating element.

However, the 1D models considered for this work are not suitable to describe coupling existing between lateral and thickness modes as they occur in array elements or even in a single-element transducer [44]. In this experiment, the FEM mode 2 did not show neutral lines, which may be not a radial mode. Both the actual vibration modes and the detailed coupling relationship need a further investigation with the help of the exact equations of radial modes for annular disks. Even so frequency measurements are precise, the approximate 1D model is not accurate enough. When s_{13}^E is introduced into modelling for 3D characterizing piezoelectric materials, the conclusions are very different [45]. Therefore, investigating the coupling relationships between lateral and thickness modes in arrays used in acoustical imaging is the next work for the PZT–NC piezoceramics before applications.

5 Conclusions

For the PZT–NC piezoceramics, its radial resonance frequency spectra were systematically investigated by both impedance measurement and theoretical analysis. Main conclusions can be drawn as follows. (1) A set of 6-parameter resonance frequency spectra are used to perform the accurate calculation of some material constants and planar coupling factors for the circular disk specimen, and the position relations between fundamental resonance and antiresonance frequencies are depicted by a new-form Nyquist diagram. (2) The frequency dependence of the AC conductivity follows the double power law above the antiresonance frequency and the conductivity at resonance/antiresonance can be calculated from the equivalent circuit parameters.

(3) Both the impedance and phase response curves are well fitted by the Van Dyke circuit model and then the equivalent circuit parameters are successfully determined from the fitting result. (5) For the annular disk specimen, the resonant behavior may be involved as a coupling between two radial modes; however, a further investigation requires to be considered in the 3D models.

Acknowledgements

This work was supported by the China Postdoctoral Science Foundation Funded Project (2017M623025), Special Funding for Post-Doctoral Research Projects from Sichuan Province (2017, presided over by Yu Chen), National Natural Science Foundation of China (Grant No. 11702037), and Opening Project of Key Laboratory of Inorganic Functional Materials and Devices, Chinese Academy of Sciences (Grant No. KLIFMD201703).

References

[1] Haertling GH. Ferroelectric ceramics: History and technology. *J Am Ceram Soc* 1999, **82**: 797–818.

[2] Zhang ST, Kounga AB, Aulbach E, *et al*. Giant strain in lead-free piezoceramics $Bi_{0.5}Na_{0.5}TiO_3$–$BaTiO_3$–$K_{0.5}Na_{0.5}NbO_3$ system. *Appl Phys Lett* 2007, **91**: 112906.

[3] Hayati R, Bahrevar MA, Ganjkhanlou Y, *et al*. Electromechanical properties of Ce-doped $(Ba_{0.85}Ca_{0.15})(Zr_{0.1}Ti_{0.9})O_3$ lead-free piezoceramics. *J Adv Ceram* 2019, **8**: 186–195.

[4] Moriwake H, Konishi A, Ogawa T, *et al*. Polarization fluctuations in the perovskite-structured ferroelectric $AgNbO_3$. *Phys Rev B* 2018, **97**: 224104.

[5] Shrout TR, Zhang SJ. Lead-free piezoelectric ceramics: Alternatives for PZT? *J Electroceram* 2007, **19**: 113–126.

[6] Panda PK, Sahoo B. PZT to lead free piezo ceramics: A review. *Ferroelectrics* 2015, **474**: 128–143.

[7] Haq M. Application of piezo transducers in biomedical science for health monitoring and energy harvesting problems. *Mater Res Express* 2018, **6**: 022002.

[8] Ma JP, Chen L, Wu Z, *et al*. Pyroelectric $Pb(Zr_{0.52}Ti_{0.48})O_3$ polarized ceramic with strong pyro-driven catalysis for dye wastewater decomposition. *Ceram Int* 2019, **45**: 11934–11938.

[9] Manjón-Sanz AM, Dolgos MR. Applications of piezoelectrics: Old and new. *Chem Mater* 2018, **30**: 8718–8726.

[10] Sherrit S, Masys TJ, Wiederick HD, *et al*. Determination of the reduced matrix of the piezoelectric, dielectric, and elastic material constants for a piezoelectric material with C∞ symmetry. *IEEE T Ultrason Ferr* 2011, **58**: 1714–1720.

[11] Sherrit S, Gauthier N, Wiederick HD, *et al*. Accurate evaluation of the real and imaginary material constants for a piezoelectric resonator in the radial mode. *Ferroelectrics* 1991, **119**: 17–32.

[12] Alemany C, Pardo L, Jimenez B, *et al*. Automatic iterative evaluation of complex material constants in piezoelectric ceramics. *J Phys D: Appl Phys* 1994, **27**: 148–155.

[13] Pardo L, Algueró M, Brebøl K. A non-Standard shear resonator for the matrix characterization of piezoceramics and its validation study by finite element analysis. *J Phys D: Appl Phys* 2007, **40**: 2162–2169.

[14] Pardo L, Montero de Espinosa F, García A, *et al*. Choosing the best geometries for the linear characterization of lossy piezoceramics: Study of the thickness-poled shear plate. *Appl Phys Lett* 2008, **92**: 172907.

[15] Rupitsch SJ, Lerch R. Inverse method to estimate material parameters for piezoceramic disc actuators. *Appl Phys A* 2009, **97**: 735–740.

[16] Pérez N, Andrade MAB, Buiochi F, *et al*. Identification of elastic, dielectric, and piezoelectric constants in piezoceramic disks. *IEEE T Ultrason Ferr* 2010, **57**: 2772–2783.

[17] Pérez N, Buiochi F, Brizzotti Andrade M, *et al*. Numerical characterization of piezoceramics using resonance curves. *Materials* 2016, **9**: 71.

[18] Chen Y, Wen YM, Li P. Characterization of PZT ceramic transducer embedded in concrete. *Sensor Actuat A: Phys* 2006, **128**: 116–124.

[19] Yang YW, Liu H, Annamdas VGM, *et al*. Monitoring damage propagation using PZT impedance transducers. *Smart Mater Struct* 2009, **18**: 045003.

[20] Chen Y, Xie SX, Wang QY, *et al*. Correlation between microstructural evolutions and electrical/mechanical behaviors in Nb/Ce co-doped $Pb(Zr_{0.52}Ti_{0.48})O_3$ ceramics at different sintering temperatures. *Mater Res Bull* 2017, **94**: 174–182.

[21] Chen Y, Xu JG, Xu Q, *et al*. Ferroelastic domain switching and R-curve behavior in lead zirconate titanate (Zr/Ti = 52/48)-based ferroelectric ceramics. *J Am Ceram Soc* 2020, **103**: 1067–1078.

[22] Zhou DY, Kamlah M, Munz D. Uniaxial compressive stress dependence of the high-field dielectric and piezoelectric performance of soft PZT piezoceramics. *J Mater Res* 2004, **19**: 834–842.

[23] Butt Z, Pasha RA. Effect of temperature and loading on output voltage of lead zirconate titanate (PZT-5A) piezoelectric energy harvester. *IOP Conf* 2016, **146**: 012016.

[24] Erhart J, Půlpán P, Pustka M. *Piezoelectric Ceramic Resonators*. Springer International Publishing, 2017.

[25] Onoe M, Gillis J. Tables of modified quotients of Bessel functions of the first kind for real and imaginary arguments. *Phys Today* 1959, **12**: 50–51.

[26] Van Dyke KS. The piezo-electric resonator and its equivalent network. *Proc IRE* 1928, **16**: 742–764.

[27] Terunuma K, Nishigaki S. A method for measuring the equivalent circuit elements for a piezo-resonator. *Jpn J Appl Phys* 1983, **22**: 143.

[28] Sutliff RW. The effects of loading on equivalent electric

circuit models for piezoelectric transducers. Miami University, 2018.

[29] Warner AW, Berlincourt D, Meitzler AH, *et al*. IEEE standard on piezoelectricity (ANSI/IEEE standard 176-1987). Technical Report. The Institute of Electrical and Electronics Engineers, Inc, 1988.

[30] Zhang YK, Lu TF, Peng YX. Three-port equivalent circuit of multi-layer piezoelectric stack. *Sensor Actuat A: Phys* 2015, **236**: 92–97.

[31] Karlash VL. Energy losses in piezoceramic resonators and its influence on vibrations' characteristics. *Electron Commun* 2014, **19**: 82–93.

[32] Albareda A, Pérez R, García JE, *et al*. Nonlinear elastic phenomena near the radial antiresonance frequency in piezoceramic discs. *J Electroceram* 2007, **19**: 427–431.

[33] Karlash VL. Modeling of the energy-loss piezoceramic resonators by electric equivalent networks with passive elements. *Mathematical Modeling and Computing* 2014, **1**: 163–177.

[34] Yimnirun R, Ananta S, Chamunglap S. Dielectric properties of $(1–x)Pb(Zr_{0.52}Ti_{0.48})O_3–(x)BaTiO_3$ ceramics under uniaxial compressive pre-stress. *Mater Chem Phys* 2007, **102**: 165–170.

[35] Damjanovic D, Rossetti Jr. GA. Strain generation and energy-conversion mechanisms in lead-based and lead-free piezoceramics. *MRS Bull* 2018, **43**: 588–594.

[36] UFFC. 177-1966-Standard definitions and methods of measurements for piezoelectric vibrators. 1966.

[37] Weaver PM, Stevenson T, Quast T, *et al*. High temperature measurement and characterisation of piezoelectric properties. *J Mater Sci: Mater Electron* 2015, **26**: 9268–9278.

[38] González A, García Á, Benavente-Peces C, *et al*. Revisiting the characterization of the losses in piezoelectric materials from impedance spectroscopy at resonance. *Materials* 2016, **9**: 72.

[39] Morrison FD, Sinclair DC, West AR. Characterization of lanthanum-doped Barium titanate ceramics using impedance spectroscopy. *J Am Ceram Soc* 2001, **84**: 531–538.

[40] Nayak P, Badapanda T, Singh AK, *et al*. Possible relaxation and conduction mechanism in W^{6+} doped $SrBi_4Ti_4O_{15}$ ceramic. *Ceram Int* 2017, **43**: 4527–4535.

[41] Atif M, Nadeem M. Interplay between the ferromagnetic and ferroelectric phases on the magnetic and impedance analysis of $(x)Pb(Zr_{0.52}Ti_{0.48})O_3–(1–x)CoFe_2O_4$ composites. *J Alloys Compd* 2015, **623**: 447–453.

[42] Funke K. Jump relaxation in solid electrolytes. *Prog Solid State Chem* 1993, **22**: 111–195.

[43] Mezheritsky AV. Elastic, dielectric, and piezoelectric losses in piezoceramics: How it works all together. *IEEE T Ultrason Ferr* 2004, **51**: 695–707.

[44] Brissaud M. Three-dimensional modeling of piezoelectric materials. *IEEE T Ultrason Ferr* 2010, **57**: 2051–2065.

[45] Brissaud M. Characterization of rectangular and cylindrical piezoceramics using three dimensional modelling. *Ferroelectrics* 2016, **500**: 259–275.

[46] Huang CH, Ma CC, Lin YC. Theoretical, numerical, and experimental investigation on resonant vibrations of piezoceramic annular disks. *IEEE T Ultrason Ferr* 2005, **52**: 1204–1216.